



HAL
open science

Subsidence of the lava flows emitted during the 2012–2013 eruption of Tolbachik (Kamchatka, Russia): Satellite data and thermal model

M.S. Volkova, N.M. Shapiro, O.E. Melnik, V.O. Mikhailov, P.Yu. Plechov,
E.P. Timoshkina, O.V. Bergal-Kuvikas

► **To cite this version:**

M.S. Volkova, N.M. Shapiro, O.E. Melnik, V.O. Mikhailov, P.Yu. Plechov, et al.. Subsidence of the lava flows emitted during the 2012–2013 eruption of Tolbachik (Kamchatka, Russia): Satellite data and thermal model. *Journal of Volcanology and Geothermal Research*, 2022, 427, pp.107554. 10.1016/j.jvolgeores.2022.107554 . insu-03656249

HAL Id: insu-03656249

<https://insu.hal.science/insu-03656249v1>

Submitted on 20 Jul 2023

HAL is a multi-disciplinary open access archive for the deposit and dissemination of scientific research documents, whether they are published or not. The documents may come from teaching and research institutions in France or abroad, or from public or private research centers.

L'archive ouverte pluridisciplinaire **HAL**, est destinée au dépôt et à la diffusion de documents scientifiques de niveau recherche, publiés ou non, émanant des établissements d'enseignement et de recherche français ou étrangers, des laboratoires publics ou privés.

39 pyroclastic deposits needed for the evaluation of the volcanic effusion rates (e.g., Poland 2014;
40 Dai and Howat, 2017).

41 Post-emplacment deformation of the lava deposits is one of the key processes affecting the
42 evolution of the ground elevation in volcanic areas. The related subsidence may reach metric
43 values and they are observable even several years after the eruptions (e.g., Briole et al., 1997;
44 Wittmann et al., 2017; Chen et al., 2018; Carrara et al., 2019). A spectacular example is the
45 observation of up to 5 cm/year subsidence rate in the Parícutin lava field ~60 years after the
46 eruption (Chaussard, 2016). This process is often described with models including the thermal
47 cooling and compaction (Wittmann et al., 2017; Carrara et al., 2019) and the viscous relaxation of
48 the lava substrate (Briole et al., 1997). Developing and verifying accurate approaches for
49 predicting the lava deposits deformation is important for several reasons. First, this strong
50 deformation can mask signals from the deep activity of the plumbing system and, therefore, should
51 be corrected for. Second, the deposit compaction should be accounted for when estimating their
52 volumes and the related effusive rates. Detailed thermal modelling and comparison of the predicted
53 and real lava surface subsidence rates obtained from SAR interferometry makes it possible to
54 constrain such model parameters as mineralogical composition, temperature of phase transition,
55 thickness, porosity, and rate of growth of lava layer. Finally, the modeling of the currently ongoing
56 deformation can be used to estimate thicknesses and volumes of the old lava flows deposited before
57 the satellite methods based on DEM measurements became available (Chaussard, 2016).

58 Many studies were devoted to modeling of the thermal cooling of a lava flow during volcanic
59 eruptions of various types and to subsequent subsidence of the lava surface. Models differ in their
60 complexity and a range of thermal parameters. Shaw et al (1977) suggested a thermal model of the
61 Hawaiian Alae lava lake and compared the synthetic temperature field with the measured
62 temperature profiles obtained by drilling of the solidified lava crust by (Peck, 1978). By comparing
63 1D and 2D solutions Shaw et al. (1977) demonstrated that a one-dimensional model is sufficient
64 for an adequate thermal modeling when the ratio of the thickness of the lava flow to its horizontal
65 dimensions is small. Keszthelyi and Denlinger (1996) showed that the main mechanisms at the
66 initial stage of lava cooling are thermal radiation, natural convection at the atmosphere – lava
67 boundary, conductive heat transfer within the flow, dependence of thermophysical properties on
68 temperature and porosity, as well as release of latent heat during crystallization. Neri (1998)
69 extended this analysis considering magma as a vesiculated binary melt with a given liquidus and
70 solidus temperature and with the possible presence of a eutectic.

71 Patrick et al. (2004) considered the cooling process of the lava flow formed during the 1997
72 eruption of Okmok volcano taking into account ambient temperature fluctuations and data on
73 precipitation and wind strength. They argue that after lava has cooled for more than 2 years, one

74 of the main factors controlling the heat transfer turned out to be thermal conductivity and porosity,
75 i.e. other parameters affect the lava cooling process only at the initial stage.

76 Recently Chaussard (2016) presented a thermal model of the cooling lava to explain the
77 long-term subsidence of the of Parícutin volcano lava fields (Mexico). These lavas were deposited
78 during the eruptions of 1943 – 1952 and their subsidence was registered by interferometric
79 synthetic aperture radar (hereinafter referred to as InSAR) in ???-???. This model takes into
80 account radiation and convection from the lava surface, conductive heat transfer within the flow
81 and to the ground, vesiculation and latent heat generation during magma solidification. The
82 modeling results showed that compaction induced by cooling of a lava flow up to 200 m thick
83 explains the real subsidence of the flow, 60 years after its formation when conductive transfer to
84 the ground is considered.

85 In this paper, we study the subsidence of the basaltic lava flows deposited during the 2012-
86 2013 eruption of the Tolbachik volcano in Kamchatka, Russia (Belousov et al., 2015; Edwards et
87 al., 2015). This was one of the largest effusive eruptions occurred during recent decades that
88 emitted 0.573 km³ of basaltic lavas forming extended flows covering ~45.8 km² (Gordeev and
89 Dobretsov, 2017). This eruption was well observed with satellites resulting in accurate estimation
90 of the thickness and area of the lava deposits (Dai and Howat, 2017; Kubanek et al., 2015; Kubanek
91 et al. 2017). Here we perform a SAR interferometry analysis with a series of Sentinel-1 satellite
92 images (C-band radar, European Space Agency ESA) from 2017 to 2019 to estimate the lava field
93 surface displacement rates. These rates are then compared with the deposit thicknesses and results
94 of thermal modeling.

95 Tolbachik is an active volcano in the Klyuchevskoy Volcanic Group (KVG) located in the
96 northern termination of the Kuril Kamchatka subduction zone (inset in Fig. 1). KVG is one of the
97 largest and most active volcanic centers in the World (e.g. Shapiro et al., 2017a) that contains 13
98 large strato-volcanoes three of which, Klyuchevskoy, Bezymianny and Tolbachik, have been very
99 active in the past few decades. Accumulated scientific evidences suggest that these volcanos might
100 be connected by a deep and extended plumbing system (e.g., Fedotov et al., 2010; Shapiro et al.,
101 2017b; Koulakov et al., 2020; Coppolla et al., 2021). The KVG eruptions are very frequent with
102 some major events such as the Great Tolbachik Fissure Eruption (GTFE) in 1975-1976 (Fedotov,
103 1984) and the Tolbachik Fissure Eruption in 2012-2013, named after the 50th anniversary of the
104 Institute of Volcanology and Seismology Far-East Branch of Russian academy of sciences (FEB
105 RAS), TFE-50.

106 TFE-50 began on November 27, 2012, and lasted nearly 10 months, until September 15,
107 2013. Initially, on the southern slope of the Plosky Tolbachik volcano, a 6 km long radial fissure
108 was formed, oriented to the SSW. The fissure began at an altitude of about 2100 m and descended

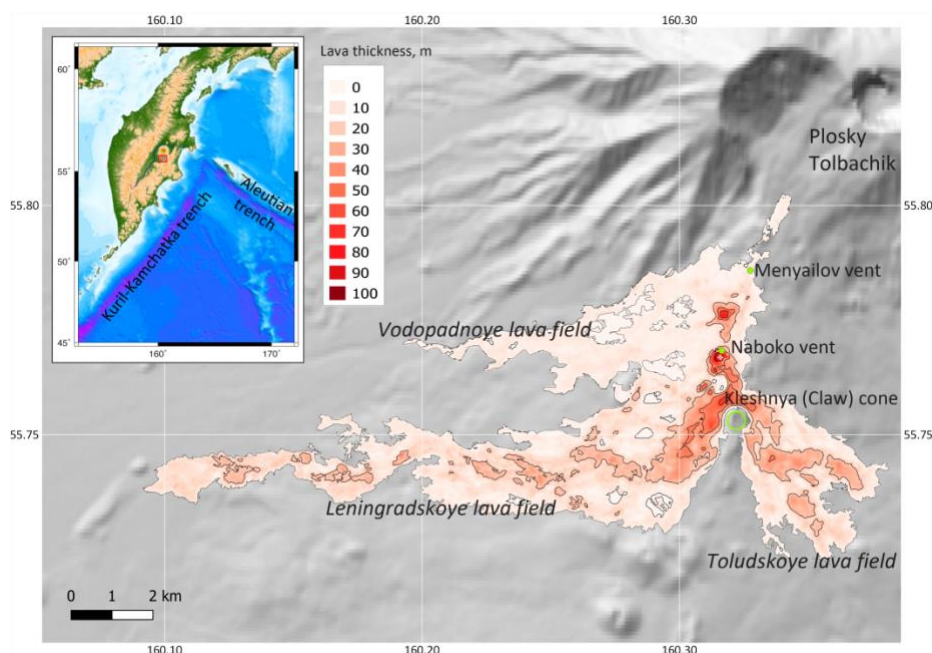
109 to an altitude of 1500 m. At first, lava spouting along the entire length of the fissure was observed,
110 then after a few hours the eruption localized in two vents at altitudes of 2000 and 1600 m, named
111 after Kamchatka volcanologists as the Menyaylov and Naboko Vents (Gordeev, Dobretsov, 2017).

112 The lava flow from the Menyaylov Vent divided into two main flows: the Vodopadny and
113 Leningradsky flows (Fig. 1). Each of them was about 10 km long. The Menyaylov Vent, which
114 was located higher, ceased its activity by December 1, 2012. Since then, the eruption occurred
115 only from the lower Naboko Vent. By December 13, 2012, the length of the Leningradsky flow
116 reached 16 km, and its thickness on the lateral and frontal parts was estimated as 3 - 15 m. When
117 the Leningradsky flow reached the Kleshnya cone, a smaller Toludsky flow separated from it and
118 ran south-eastward. The Toludsky flow from the Naboko Vent is 5 km long, and it stopped at an
119 altitude of about 1100 m (Belousov et al., 2015).

120 The most voluminous Leningradsky lava field started to form from the first days of the
121 eruption with an average lava flow rate of $140 \text{ m}^3 / \text{s}$ during the first two weeks. The second
122 important Toludsky field began to form from December 22 to 23 by a flow enveloping the lava
123 pile that was formed upslope of the Kleshnya cone (Fig. 1). From the second half of December,
124 the eruption was steady, with an average lava flow rate of $18\text{-}19 \text{ m}^3 / \text{s}$. The formation of both the
125 Leningradsky and Toludsky fields was greatly influenced by lava channels and tubes (Dvigalo et
126 al., 2013).

127 Fig. 1 shows the thickness map of the lava field constructed from data provided by Dai and
128 Howat (2017). The authors assessed the lava thickness by differentiating two DEMs produced
129 before and after the eruption using data from ArcticDEM, a highly accurate sub-meter resolution
130 DEM that covers the entire Arctic region.

131



132

133 **Figure 1.** Thickness of the lava flows (in meters) formed as a result of TFE-50 according to (Dai,
134 Howat, 2017). The base map is the SRTM digital elevation model. The inset shows the location of
135 Tolbachik in the Kamchatka Peninsula.

136

137 We use a series of Sentinel-1 SAR images from 2017 to 2019 to estimate the lava field
138 surface displacement rates. Then, we develop a mathematical model for the magma cooling
139 process and obtain governing parameters that provide the best consistency with data on the lava
140 surface subsidence during its solidification. Our model takes into account the latent heat of
141 crystallization, temperature dependences of physical parameters (heat capacity, thermal
142 conductivity, density), temperature dependence of crystal concentration in the melt volume, and
143 the percentage of uncrystallized material (glasses), porosity and lava layer formation rate.

144

145 **2. Estimation of lava surface displacements by SAR interferometry**

146 Measurement of the displacements of the earth's surface or man-made objects by satellite
147 radar interferometry methods are based on the differential analysis of images taken by a synthetic
148 aperture radar (SAR) for the same segments of the earth's surface. The radar emits an
149 electromagnetic signal at a certain angle to the vertical, called the off-nadir angle, and receives the
150 signal reflected from the earth's surface. The amplitude and phase of the reflected signal are
151 recorded for each resolution element. Based on the phase shift of the signals received during the
152 first and second surveys, we can estimate the displacements of the reflecting natural or man-made
153 object during the time interval between two surveys (Hanssen, 2001).

154 Depending on the problem to be solved, researchers use methods based on analysis of a pair
155 of images (so-called differential interferometry, DInSAR) or a series of interferograms in which
156 so-called persistent scatterers (PS) are identified and their average displacement rates are measured
157 using time series approaches (e.g., Ferretti et al., 2001). The former allows us to estimate surface
158 deformations with a centimetric accuracy and the average displacement rates over the time series
159 can be estimated at a few mm/yr.

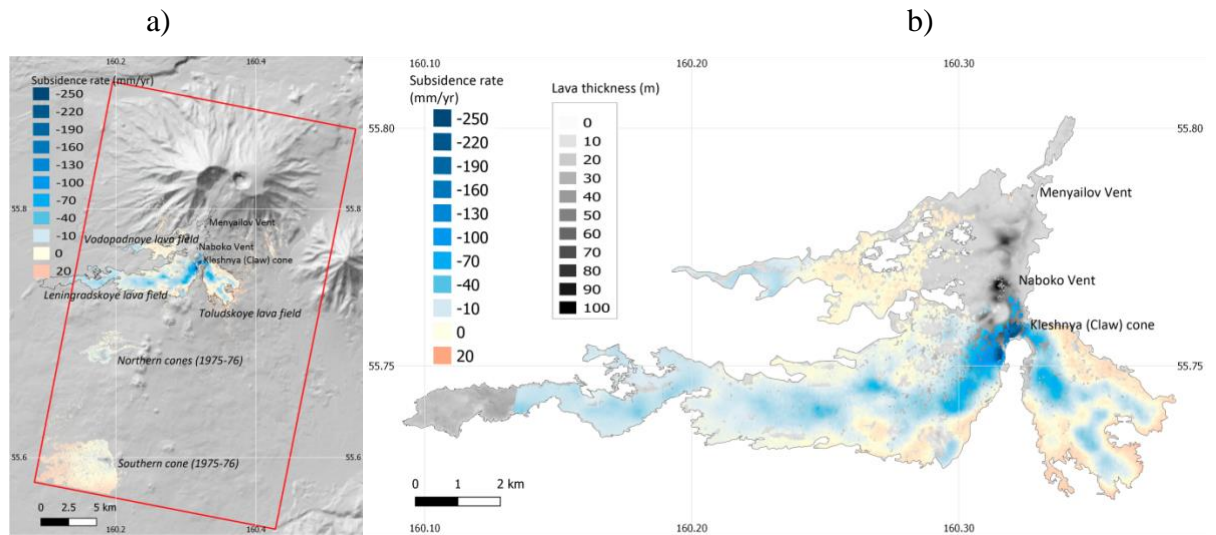
160 An important indicator that controls the quality of the results obtained is the interferometric
161 correlation of the images (coherence), which varies from 0 to 1. With low coherence (usually <0.2-
162 0.3), it is difficult to combine (co-register) images and then assess displacements. When studying
163 Kamchatka, we cannot always find pairs of images with a good correlation due to the peculiarities
164 of the region, such as mountainous terrain, the presence of snow for most of the year, rapidly
165 changing vegetation in summer, and active surface processes. Nevertheless, the SAR
166 interferometry method has been successfully used to monitor volcanoes, including those on the
167 Kamchatka Peninsula. Successful examples include the study of surface displacements in the Uzon

168 caldera studied by (Lundgren and Lu, 2006), displacements of the slopes of Kizimen (Ji et al.,
169 2013), Tolbachik (Lundgren et al., 2015, Kubanek et al., 2015; Kubanek et al. 2017), Karymsky
170 (Ji et al., 2018), Bezymianny (Mania et al., 2019), Bolshaya Udina (Senyukov et al., 2020) and
171 Koryaksky (Mikhailov et al., 2022) volcanoes were studied.

172 To assess the surface displacements of the Tolbachik lava fields, we processed a time series
173 of radar images using the Small Baseline Subset technique (SBAS, (Berardino et al., 2002)) in the
174 SARscape software. We used 35 Sentinel-1A satellite images taken in Interferometric Wide Swath
175 mode from the 60th track of descending orbit during the snow-free period of 2017-2019: from
176 May 14, 2017 to September 23, 2017 (12 images), from May 21, 2018 to September 30, 2018 (12
177 images) and from May 16, 2019 to September 13, 2019 (11 images).

178 In the SBAS technology, the available set of images is used to make all possible
179 combinations of pairs whose spatial and temporal baselines do not exceed specified thresholds.
180 For the Kamchatka region we set them equal to 100 m and 4 - 4.5 months. From the selected pairs,
181 the stack of interferograms and their absolute phases are calculated. Once the phase values are
182 known, the next step is to reconstruct the sequential dynamics of the displacements over time. It
183 is followed by spatial and temporal filtering to eliminate atmospheric delay. This method is
184 effective for natural weakly reflective terrains (Berardino et al., 2002; Lanari et al., 2004). It is
185 also convenient because it does not impose strict requirements for the number of images in a time
186 series, which is very important for the harsh environment of the Kamchatka region.

187 The SAR interferometry methods determine the displacements by the phase difference of
188 the reflected signals, so the resulting displacements are equal to the projection of the total
189 displacement vector in the direction along the Line Of Sight (LOS) (Hanssen, 2001). If the
190 displacements in the horizontal directions can be approximated as negligible (as is the case with
191 cooling lava flows), with knowing the incidence angle of the satellite beam, we can calculate the
192 displacements in the vertical direction, which we will call subvertical. According to the results of
193 interferometric processing by the SBAS method, the maximum rates of subvertical displacements
194 of the lava layer surface are in the region of the Kleshnya cone and have a value of 285 mm/yr for
195 2017, 249 mm/yr for 2018, and 261 mm/yr for 2019. The surface subsidence rates of the central
196 and lower parts of the field do not exceed 80 mm/yr. In general, the Leningradsky field subsides
197 slightly faster than the Toludsky field (Fig. 2).



199

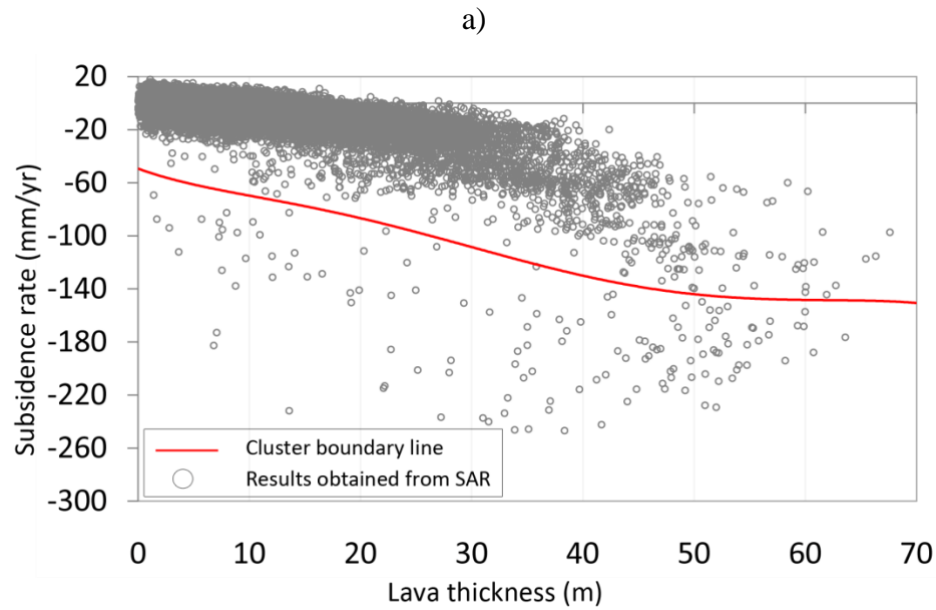
200 **Figure 2.** (a) Map of observed lava surface displacement rates inferred from SAR interferometry
 201 and averaged between 2017 and 2019. The red rectangle outlines the study area. (b) The same
 202 map compared with the lava thickness (Dai and Howat, 2017).

203

204 It should be noted that interferometric processing did not allow us to obtain a continuous
 205 map of surface displacement rates for the entire region occupied by the lava flows because of the
 206 difficult terrain and loss of coherence higher up the slope. Therefore, the lava field thickness values
 207 comparable with the results obtained for the lava subsidence values from satellite data lie in the
 208 range from about 0 to 60 meters. The maximum thickness of the lava field, obtained by
 209 ArcticDEM, reaches almost 100 meters and is located in the vicinity of the Naboko cone (Fig. 2).

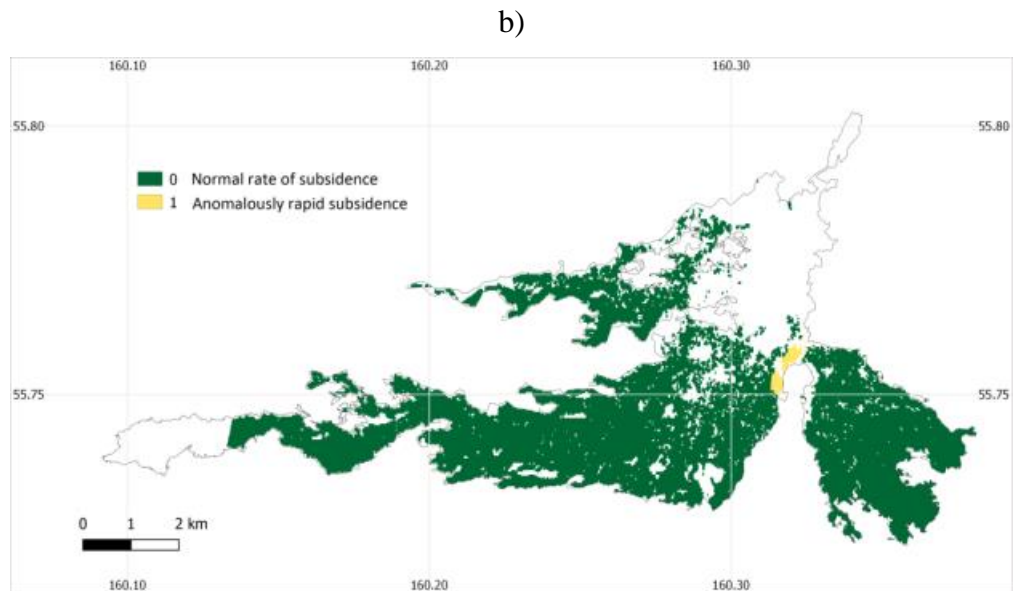
210 The subsidence rates for all points with measurements are compared with the lava thickness
 211 in Fig. 3a. A clear trend can be identified as dense point cloud in the upper part of this plot.
 212 Following this trend, the subsidence rate is proportional to the thickness and reaches values of
 213 ~100 mm/year for the flow thickness about 60-70 m. At the same time, a separate group of points
 214 with "anomalously" high values of the lava surface subsidence (up to 260 mm/yr) can be clearly
 215 distinguished from the main "cluster". We separate two "clusters" with drawing a limit based on
 216 a simple visual inspection (red line in Fig. 3a) and plot them with two distinct colors in a map (Fig.
 217 3b). As a result, we see that all "anomalous" points are concentrated in a small area close to the
 218 Naboko vent and Kleshnya cone while most of the surface of the lava field subsides "normally".

219



220

221



222

223

224 **Figure 3.** (a) Comparison of subsidence rates measured from SAR data with the lava thickness.

225 Red line defines the boundary between the “normal” and “anomalous” clusters. (b) Geographical

226 locations of points with normal (green) and anomalous (yellow) subsidence rates.

227

228 At the periphery of the lava flow, especially on the Toludskoe field, SAR data shows small

229 uplift with the rate up to 18 mm/year. Slow upward movements were also registered on the slopes

230 of Tolbachik volcano above the TTI-50 lava fields and on the Southern cone at the southern edge

231 of the study area (Fig. 2a). Several processes can be responsible for the regional uplift including

232 lava migration below the Tolbachik volcano. Uplift at the border of the lava field at least partly

233 may be result of the horizontal heat transfer in the ground below the lava field from the central

234 parts where temperature is high down to 50 m depth to the relatively cold ground at the periphery
 235 of the lava field (see Fig. 5c).

236

237 **3. Model of the lava flow cooling**

238 **3.1 General model formulation**

239 We consider the cooling of a lava layer, which consists of three components: liquid melt,
 240 gas, and solid crystals. Most of the gas was released during the eruption (Plechoy et al., 2015), so
 241 the degassing of a stagnant lava flow can be ignored as a first order approximation. Following the
 242 detailed analysis in (Patrick et al., 2004), we can also ignore the process of convective heat and
 243 mass transfer. When the lava crust cools below the solidus temperature, we can ignore the heat
 244 radiation from its surface compared to the convective heat flux. We will consider the lava flow as
 245 an inherently homogeneous medium consisting of a magmatic melt and some initial volume of
 246 crystals. Strictly speaking, weight of the loading mass also leads to compaction and subsidence.
 247 But seven years after lava emplacement this process can be ignored.

248 Horizontal dimensions of the flow are significantly larger than the vertical, and a small
 249 parameter equal to the ratio of the lava flow thickness to its length can be introduced.
 250 Dimensionless analysis shows that the temperature derivatives along the horizontal coordinates
 251 are much smaller compared to the vertical one. Therefore, the horizontal temperature changes can
 252 be ignored, and we can solve the one-dimensional problem along the vertical coordinate z . Many
 253 studies of stagnant lava flow cooling have also used the 1D formulations (Neri, 1998; Shaw et al.,
 254 1977; Patrick et al., 2004, Chaussard, 2016).

255 According to the physical properties, the modelled medium is divided into a lava layer and
 256 an underlying rock layer. To discretize the modeling domain, we introduce a grid of elements with
 257 a step $\Delta z_i(t)$, $i = 1, \dots, N$; where N is the number of grid elements that determines the size of the
 258 model. The Oz axis is directed downward, and the origin of coordinates is aligned with the bottom
 259 of the lava layer.

260 As the phase change (formation of crystals from the melt) is accompanied by the latent heat
 261 release during lava cooling, the problem results in solving a 1D energy equation with advection
 262 due to subsidence and volumetric heat source:

$$263 \quad \frac{\partial T}{\partial t} = \frac{\partial}{\partial z} \left(k \frac{\partial T}{\partial z} \right) + W(z, t) \frac{\partial T}{\partial z} + Q(z, t, T) \quad (1)$$

264 with initial and boundary conditions:

$$265 \quad T(z, t = 0) = \begin{cases} T_{melt}; & \text{for } z \in [-H_{ini}; 0]; \\ dT_0 * z; & \text{for } z \in (0; H_{max}]; \end{cases} \quad (2)$$

$$266 \quad T(-H_{ini}, t) = 0; T(H_{max}, t) = dT_0 * H_{max},$$

267 where $T(z, t)$ and $W(z, t)$ are the temperature and subsidence rate of the lava at the depth z at time
 268 t ; $Q(z, t, T) = L/c_p * \partial X_{faz}(z, T)/\partial t$ is the amount of the latent heat released per unit volume
 269 during the phase change (crystallization); $X_{faz}(z, T)$ is the proportion of the solid phase at the depth
 270 z . L is the latent heat of crystallization, c_p is the specific heat capacity, and $k(t, z)$ is the thermal
 271 diffusivity. The initial thickness of the lava layer is equal to H_{ini} . The depth of the model's lower
 272 boundary, H_{max} , is set big enough to assume that temperature changes below this boundary can be
 273 ignored, T_{melt} is the initial temperature of the melt, dT_0 is the temperature gradient in the soil by
 274 the time the eruption begins.

275 Lava density depends on its composition, temperature, presence of pores, and the amount of
 276 crystallized (crystals) and uncrystallised (glass/melt) components. Let us introduce the fraction of
 277 solidified part of the lava $X(t, T)$, equal to the equilibrium fraction of crystals calculated for
 278 crystallization of the most primitive TFE-50 lava in the Petrolog 3 software (Danyushevsky,
 279 Plechov, 2011). Let X_{cr} , X_{gl} and X_{por} be the volume fractions of crystals, glass and pores (gas) in
 280 the solidified part of the lava, which we will consider independent of time and temperature: $X_{cr} +$
 281 $X_{gl} + X_{por} = 1$. The molten part consists of magmatic melt and gas in the pores, with the porosity
 282 of the melt being also equal to X_{por} . These are average values for the flow thickness, although in
 283 the upper part (crust) and the massive main part the fractions of pores and crystals will be different.

284 We will consider X_{gl} and X_{por} to be free parameters, and adjust their values by comparison
 285 with the data on the lava surface subsidence. We used the following parameters as the initial ones:

$$286 \quad X_{gl} = 0.2, X_{por} = 0.1, \text{ then } X_{cr} = 1 - (X_{gl} + X_{por}) = 0.7.$$

287 The density of molten part of lava (ρ_{lava}) is:

$$288 \quad \rho_{lava}(t, T_{melt}) = \rho_{melt} * (1 - X_{por}) + \rho_{por}(t, T) * X_{por},$$

289 where ρ_{melt} is the density of the melt, ρ_{por} is the density of the gas filling the pores.

290 The solidified part consists of crystals with the density $\rho_{cr}(t, T)$, glass with the density
 291 $\rho_{gl}(t, T)$ and gas in the pores ($\rho_{por}(t, T)$). Then the density of the solidified part - ρ_{solid} , is:

$$292 \quad \rho_{solid}(t, T) = \rho_{cr}(t, T) * X_{cr} + \rho_{gl}(t, T) * X_{gl} + \rho_{por}(t, T) * X_{por} ,$$

293 and the density of the lava containing the melt and the solidified part (both with the gas fraction
 294 X_{por}) is:

$$295 \quad \rho_{total}(t, T) = \rho_{solid}(t, T) * X(t, T) + \rho_{lava}(t, T) * (1 - X(t, T)).$$

296 By substituting the densities of the lava and the solidified part here, one will get:

$$297 \quad \rho_{total}(t, T) = (\rho_{cr}(t, T) * X_{cr} + \rho_{gl}(t, T) * X_{gl} + \rho_{por}(t, T) * X_{por}) * X(t, T) \\ 298 \quad + (\rho_{melt} * (1 - X_{por}) + \rho_{por}(t, T) * X_{por}) * (1 - X(t, T)),$$

299 or after reducing the terms with $\rho_{por}(t, T)$:

300
$$\rho_{total}(t, T) = (\rho_{cr}(t, T) * X_{cr} + \rho_{gl}(t, T) * X_{gl}) * X(t, T) + \rho_{melt} * (1 - X_{por}) * (1 - X(t, T)) + \rho_{por}(t, T) * X_{por},$$
 (3)

302 Now in equation (1), the heat released during crystallization will be:

303
$$Q(z, t, T) = L/c_p * \partial X_{faz}(z, T)/\partial t = L/c_p * X_{cr} * \partial X(z, T)/\partial t$$

304 because some part of the melt transforms into glass during solidification and the energy released
305 during this process can be ignored.

306 In the modeling, the density of crystals $\rho_{cr}(t, T)$ is calculated from the equilibrium density
307 of crystal assemblage (Pl, Ol, Cpx) with account of their compositions (An, Fo and Mg#). These
308 properties were calculated in Petrolog 3 software (Fig. 4).

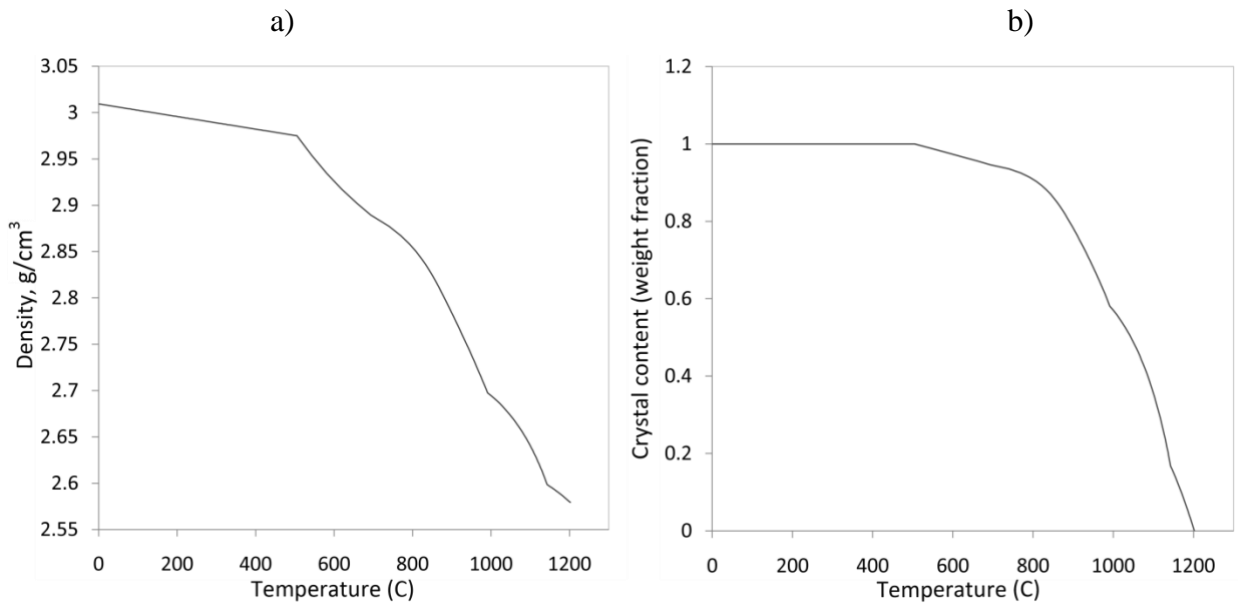
309 The glass density is close to the melt density and changes only due to cooling:

310
$$\rho_{gl}(t, T) = \rho_{melt} * (1 - \alpha_{v_glass} * (T - T_{melt}^{(0)})),$$

311 where α_{v_glass} stands for the coefficient of thermal expansion of glass equal to $5.8*10^{-7} 1/degC$,
312 the melt density is assumed constant $\rho_{melt}=2.6428 g/cm^3$ and corresponds to the density at
313 $T_{melt}^{(0)}=1100$ °C (Fig. 4A), the gas density in the pores $\rho_{por}(t, T)$ can also be assumed constant
314 $0.001 g/cm^3$, since its contribution is negligibly small.

315

316



317

318 **Figure 4.** Temperature dependencies of magma density (g/cm^3) (a) and crystal content (weight
319 fraction) in the melt (b), as determined from laboratory data using the Petrolog 3 software
320 (Danyushevsky, Plechov, 2011).

321

322 The height of all grid elements Δz_i is recalculated at each time step due to temperature
323 changes. That allows calculation of the displacement rate $W(z, t)$ in equation (1) using conservation
324 of mass $\rho(t, T) * \Delta z(t, T) = \rho(T_{melt}) * \Delta z(T_{melt})$. Thus:

325
$$\Delta z(t, T) = \Delta z(T_{melt}) * \rho(T_{melt}) / \rho(t, T). \quad (4)$$

326 The crystal density and thermal expansion coefficient α_v depend on the crystal composition.
 327 We use a value averaged over the minerals that make up the Tolbachik lava. Below the solidus,
 328 the density is calculated as a function of temperature:

329
$$\rho_{cr}(t, T) = \rho^{(0)}(1 - \alpha_v(T(t) - T_{cr}^{(0)})), \quad (5)$$

330 with parameters $T_{cr}^{(0)} = 505^\circ\text{C}$; $\rho^{(0)}$ is equal to the equilibrium density value of 2.9752 g/sm^3 at
 331 the temperature $T_{cr}^{(0)}$. Equation (5) corresponds to the slope of the curve in Fig. 4A.

332 Porosity decreases from 54 vol. % to 6 vol. % during the flow of lava. Then, during
 333 solidification, presumably due to additional volatile release, the porosity slightly increased again
 334 to 8 vol. % (Plechov et al., 2015). In the upper parts of the flow, the porosity is relatively high (35
 335 vol. %). Individual samples of aa-lava picked up at the surface of the lava flow are similar to
 336 solidified foam, with an assessed porosity up to 75% (Gordeev, Dobretsov, 2017).

337 The model also accounts for the incremental formation of the lava flow. It is assumed that
 338 the lava layer with the thickness $H(t)$ is formed during the first year (the year of the eruption) at
 339 the constant rate dh/dt , where dh is the given increment in meters over the time dt , so that $H(t) =$
 340 $t \times dh/dt$. In the first year, a layer of cells with the given thickness dh was added to the model at
 341 the top of the flow at the equal time intervals dt until the given final thickness of the lava layer H_{fin}
 342 was reached. It was assumed that at the time t_0 the thickness of the flow is equal to H_{ini} .

343

344 **3.2 Model parameters**

345 Equations (1)-(2) are solved in the domain with dimensions: $H(t) + H_{max}$, where $H(t)$ is the
 346 thickness of the lava layer for different scenarios of its build-up dh/dt (the final thickness value
 347 H_{fin} varied from 10 to 60 meters), H_{max} is the thickness of the soil layer. The grid step along z in
 348 the lava layer is 0.1 m, the grid step along z in the soil layer (i.e. from $z=0$ to $z=H_{max}$) increases
 349 with depth, the time step is $\tau = 0.5$ of a day.

350 The initial temperature of the melt is $T_{melt} = 1100^\circ\text{C}$, the initial temperature gradient with
 351 depth in the underlying rocks before the eruption is assumed as $dT_0=50^\circ\text{C/km}$; the specific heat of
 352 crystallization $L = 3.5 \cdot 10^5 \text{ J/kg}$; the thermal expansion coefficient α_v of igneous material
 353 corresponds to the density model in Fig.4a.

354 The heat capacity c_p and thermal conductivity λ are given the following temperature
 355 dependences: for c_p (J/kg/K) according to (Patrick et al., 2004):

356
$$c_p(T) = 1100 \text{ for } T > 1010 \text{ K};$$

357
$$c_p(T) = 1211 - (1.12 \cdot 10^5)/T \text{ for } T < 1010 \text{ K};$$

358 for λ (W/m/K) according to (Hidaka et al., 2005):

359 $\lambda(T) = 1.15 + 5.9 * 10^{-7} * (T - 1200C)^2$, for $T < 1200^{\circ}C$

360 $\lambda(T) = 1.15 + 9.7 * 10^{-6} * (T - 1200C)^2$, for $T > 1200^{\circ}C$

361 The porosity and percentage content of glass were considered free parameters and selected
362 by comparing the calculated and actual data on the lava flow surface subsidence.

363 Given the year of the eruption, the modeling period t was 7 years (2012-2019). The dynamics
364 of lava flow formation and cooling is involves different physical and geological processes. In our
365 model, we focused on the thermal subsidence that plays a dominant effect in the evolution of the
366 lava flow thickness.

367

368 **3.3 Accounting for the lava thickness build-up rate**

369 We considered several scenarios for the lava layer formation for numerical modeling.
370 Because the eruption lasted 10 months, and the maximum thickness of the accumulated lava (Dai
371 and Howat, 2017) reached 100 meters (the Naboko cone region), the vertical rate of layer
372 increment dh/dt must meet these time constraints. In general, the lower the rate of layer build-up
373 dh/dt results in faster cooling and slower lava subsidence during the 7th year after the eruption. If
374 the layer builds up quickly, it cools down more slowly, resulting in a greater lava subsidence during
375 the 7th year. For the model with a growing layer, we chose two extreme scenarios: "fast" and
376 "slow". The increment thickness of the lava flow was set constant and equal to 6 meters; the same
377 thickness was set to the initial layer H_{ini} . In case of the fast formation, the lava layer grew at a rate
378 of 6 meters in 2 day, and in case of the slow formation 6 m in 20 days. These values provide time
379 intervals of lava accumulation that do not extend beyond the eruption timeline. The modeling was
380 also performed without accounting for the layer build-up, where the lava layer at time $t=0$ already
381 had the given thickness H_{fin} .

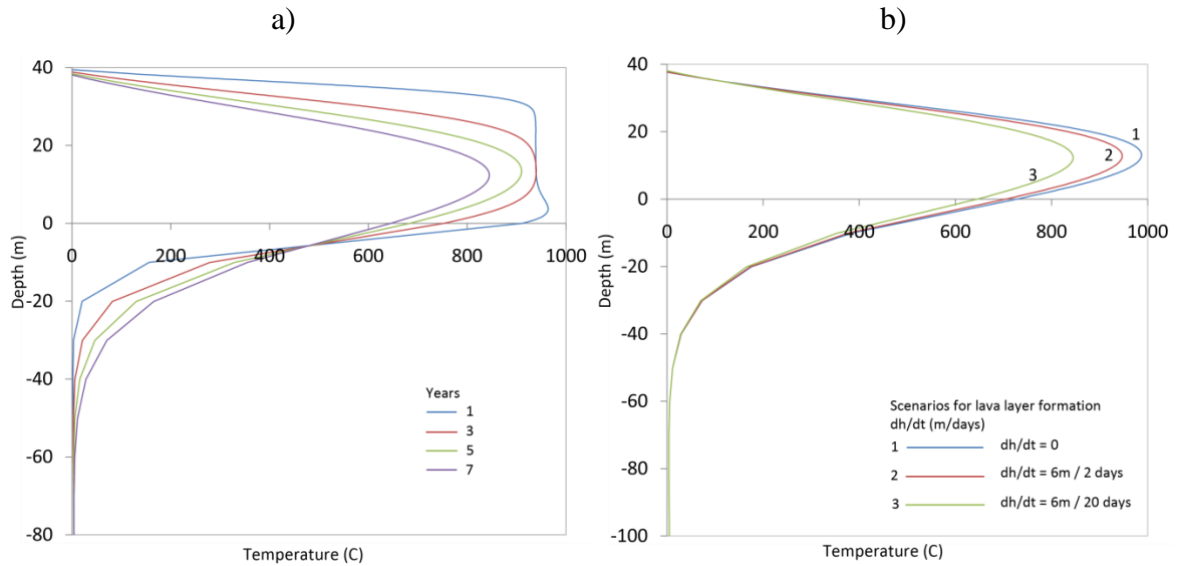
382

383 **4. Relationship between the thermal cooling and surface subsidence**

384 Fig. 5 shows temperature profiles computed assuming 10% porosity and 20% of glass and
385 different rates of lava flow emplacement. Because most of the lava field has thicknesses between
386 20 and 40 meters, we mainly consider a 40 meters thick layer. Fig. 5a shows how the temperature
387 evolves during 7 years within a 40 meters thick layer formed with $dh/dt=6m$ per 20 days. It shows
388 a progressive cooling of the lava layer and heating of the underlying crust. For such "slow"
389 scenario, the temperature at the base of the lava flow by the end of the first year is higher due to
390 the addition of new overlying layers of molten magma in the first year. Over time, lava cools down
391 and after 7 years its maximum temperature is $\sim 845^{\circ}C$, with an equilibrium crystallinity of about
392 86.7 %, implying that the crystallization process is not yet completed. Fig. 5b shows that with the
393 slow lava emplacement, the temperature in the middle of the layer by the end of the 7th year is

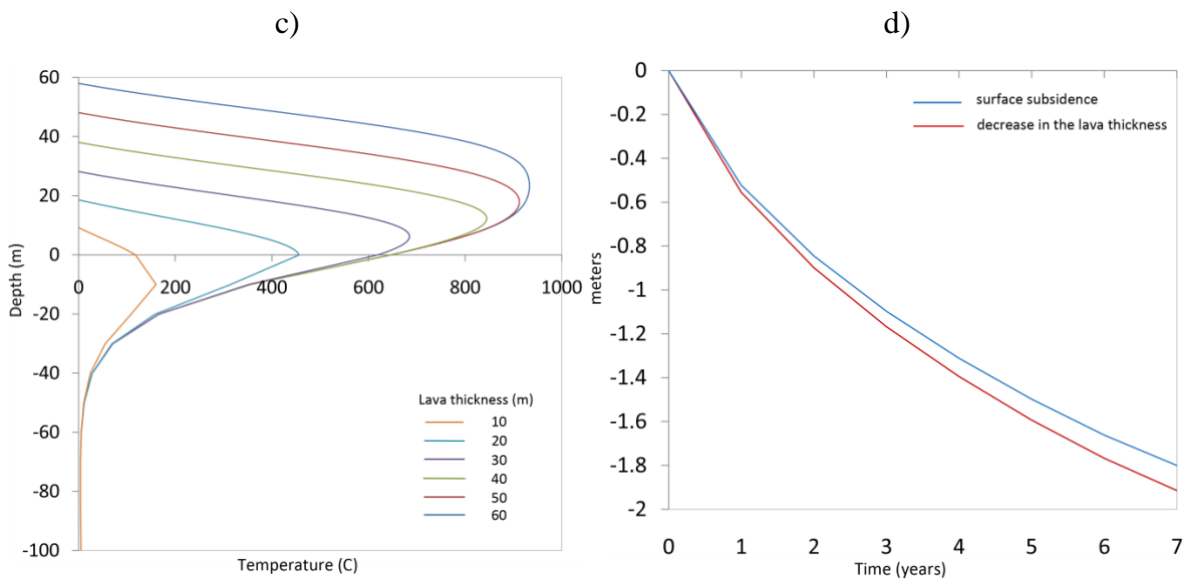
394 almost 150 °C lower than with the fast and instantaneous emplacement. Fig. 5c shows that the
395 maximum temperature in the layer depends strongly on its thickness. For a 60 meters layer, by the
396 end of the 7th year, there is still a melt in the middle of the flow. In a 30 meters layer, the
397 crystallization process in the middle of the layer is already completed after 7 years. Layers with a
398 thickness smaller than 40 m reach crystallinity >54% by the end of the 7th year after the eruption
399 and their subsidence slows down considerably. At the same time, lavas with a thickness of above
400 50 m after 7 years still contain melt layers. Time evolution of the surface displacement and the
401 lava thickness in a 40 meters lava layer are shown in Fig. 5d. Note, that the layer thinning is slightly
402 faster than the surface subsidence because of the small contribution of the heating of the underlying
403 crust.
404
405

406



407

408



409

410 **Figure 5.** (a) Temperature profiles 1, 3, 5, and 7 years after the eruption with a slow layer build-
 411 up ($dh/dt=6m$ per 20 days) and $H_{fin} = 40$ m. (b) Temperature profiles 7 years after the eruption
 412 for $H_{fin} = 40$ m for different scenarios: 1 – instantaneous layer formation ($dh/dt=0$); 2 and 3 – fast
 413 ($dh/dt=6m$ per 2 days) and slow ($dh/dt=6m$ per 20 days) growing layers, respectively. (c)
 414 Temperature profiles 7 years after the eruption for different lava flow thicknesses: H_{fin} from 10 to
 415 60 meters ($dh/dt=6$ m per 20 days). (d) Time evolution of the lava thickness and surface subsidence
 416 (red and blue colors, respectively) for a layer with: $H_{fin} = 40$ m, $dh/dt=6$ m per 20 days. A porosity
 417 of 10% and a glass content of 20% have been used in all shown simulations.

418

419 5. Comparison of the modeling with the results of SAR interferometry

420 Fig. 6 shows the comparison of the observations with the modeling results assuming
 421 different percentages of pores and glasses in the igneous material of slow flow formation at dh/dt
 422 $= 6$ m per 20 days. We use this comparison to assess the effect of porosity and glass content in the

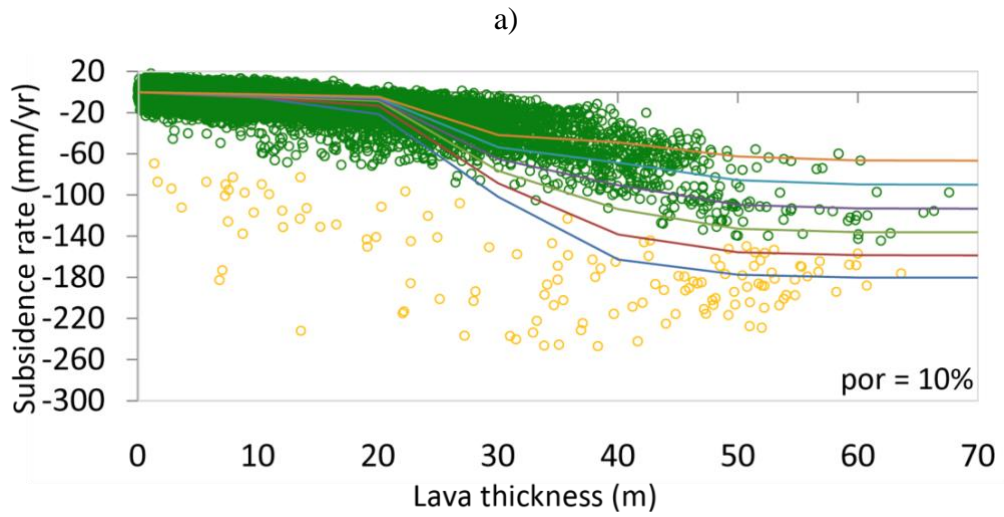
423 lava on its subsidence. Calculations in Fig.6 show that an increase in the glass quantity in the final
424 lava composition, similarly to an increase in porosity, leads to a decrease in the lava surface
425 subsidence rate during the 7th year.

426 Fig. 7 shows the results of modeling with parameters that fit well the “normal” trend of lava
427 subsidence (green circles). These curves have been obtained with considering a “slow layer build-
428 up” scenario (dh/dt 6 m during 20 days).

429 We also performed simulations with other possible rates of the lava thickness build-up. Fig.
430 8 shows the results of such modeling with 10% porosity and 20% glass content compared with the
431 observations. Scenarios of rapidly (dh/dt 6 during 2 days) or instantly formed lava layer fit better
432 the observations in the “anomalous” zone (yellow circles).

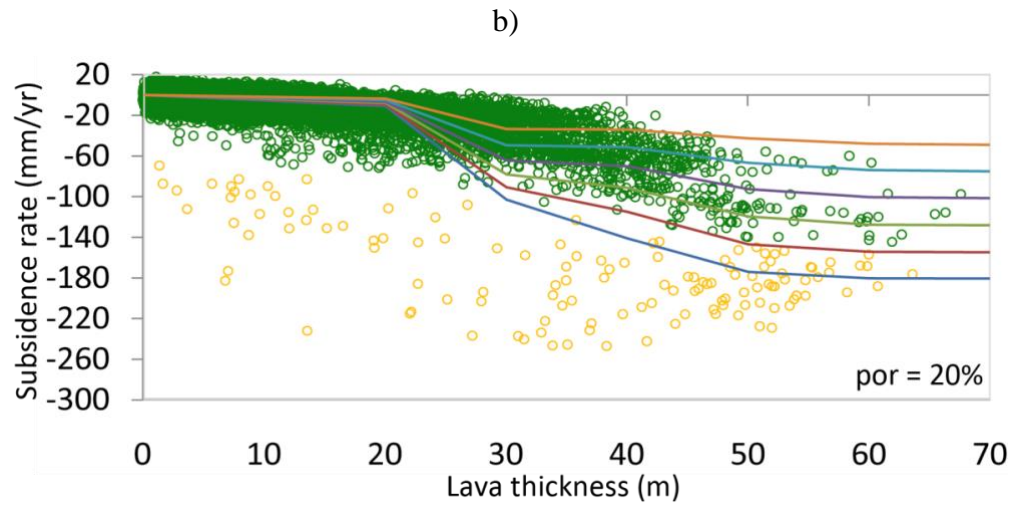
433

434



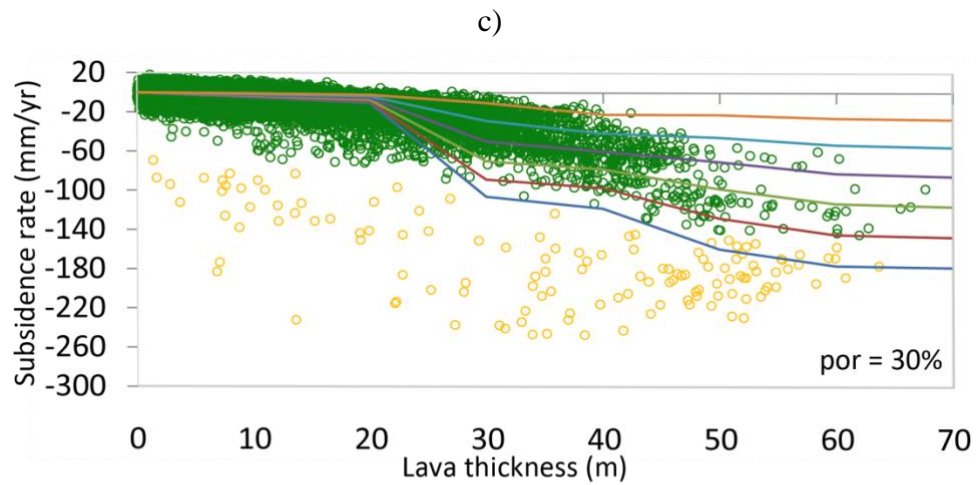
435

436



437

438



glass content (%): — 10 — 40 ○ Results obtained from SAR
— 20 — 50
— 30 — 60

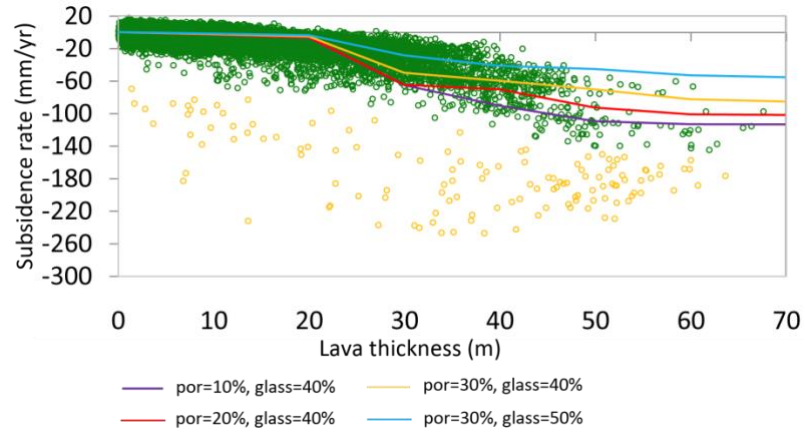
439

440 **Figure 6.** Assessment of the effect of porosity and glass content in the lava on the subsidence rate.

441 The colored curves show results of the modeling with different glass content for three different

442 values of porosity: (a) 10%, (b) 20%, (c) 30%.

443

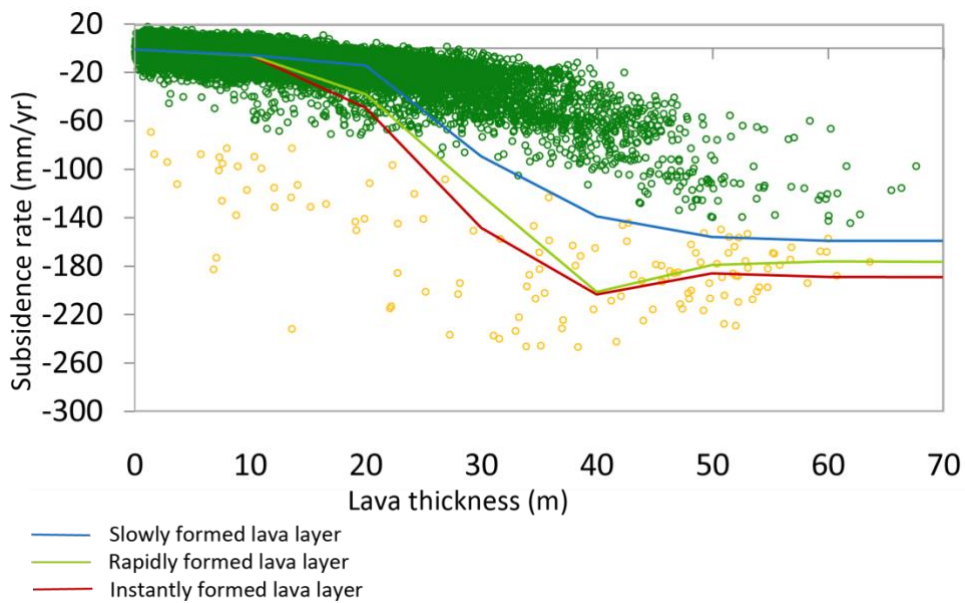


445

446 **Figure 7.** Results of the modeling with parameters best fitting the “normal” trend of the lava
 447 surface subsidence (green circles). Yellow circles are values from the “anomalous” zone of
 448 subsidence. “Slow layer build-up” scenario ($dh/dt = 6m/20d$) has been considered.

449

450



451

452 **Figure 8.** Comparison of results obtained from SAR interferometry data (green circles - “normal”
 453 rate, yellow circles - “anomalous” rate) with modeling results (colored lines) at 10% porosity and
 454 20% glass content, which better fit to “anomalous” subsidence. The vertical axis is the surface
 455 subsidence rate in 2019 (in mm/yr). The red line is the result for an instantaneous layer formation
 456 ($H_{ini}=H_{fin}$, $dh/dt = 0$). The green line is the rapidly formed lava layer ($dh/dt = 6 m$ during 2 days).
 457 The blue line is the slowly formed lava layer ($dh/dt = 6 m$ during 20 day).

458

459

6. Discussion and conclusions

460 Our observations of surface subsidence of the lava flows emitted by the 2012-2013
461 Tolbachik eruption based on SAR interferometry show two distinct trends. In more than 90 % of
462 locations, the subsidence vs. lava thickness follows the main “normal” trend that can be well
463 explained by a model based on thermal cooling and compaction of deposited lavas. So far, the
464 subsidence rate observed in the majority of the Tolbachik lava field can be directly compared with
465 those reported by Wittmann et al. (2017) who observed a ~20 mm/year vertical velocity for ~5
466 years old and ~20 m thick lava flows in Hekla, Iceland. This subsidence rate is very close to our
467 observations for the “normal” part of the Tolbachik fields (Figure 3a). The considered simple
468 model allows us to fit this main trend inferred from the satellite-based measurements of the lava
469 subsidence rates with varying just a few free parameters. The best fit to SAR data was achieved
470 for the slowly formed lava layer ($dh/dt = 6$ m during 20 day) with porosity being between 10-30%
471 and glass content between 30-50%.

472 At the same time, a relatively small number of points clearly show much faster subsidence
473 in comparison with this “normal” trend. All these “anomalous” points are located in a small
474 compact area in the vicinity of the Naboko vent and Kleshnya cone. The emergence of this region
475 with high lava surface subsidence rates can be explained by the specific conditions of lava flow
476 formation.

477 One possibility is that this part of the flow was formed very quickly after the active vent
478 opening, which is different from more distant parts of the lava fields growing more progressively.
479 Indeed, computations based on scenarios of “fast” or “instant” lava layer formation predict
480 significantly faster subsidence rates for layers thicker than 25 m (Fig.8).

481 At the same time, a considerable number of “anomalous” points are observed in the relatively
482 thin part of the flow and cannot be solely explained by the model based on thermal compaction.
483 Therefore, other processes should be considered for explaining the full range of observations.
484 During the eruption, a system of lava tubes and channels was formed in the upper part of the flow
485 just beneath the Naboko vent. These tubes were emptied during the eruption with lava flowing to
486 the outer part of the field resulting in formation of many cavities. The region of the anomalously
487 fast subsidence likely corresponds to a collapse of such “lava caves”. So far, episodes of such very
488 fast subsidence have been observed during the eruption. For example, the lava surface elevation
489 seen from the sky window southward from the Naboko cone dropped by ~5 m between February
490 and May 2013 (Gordeev, Dobretsov, 2017). Six-seven years after the eruption, a significant
491 number of large cavities are still present under the solidified top of basaltic flow in the region
492 where the satellite data measure high subsidence rates.

493 Overall, our results for the well-documented Tobachik eruption show that while most of the
494 measured lava subsidence can be well explained by a simple thermal compaction model, the largest

495 observed values can be at least in part due to other processes such as collapsing cavities within the
496 lava deposits. Therefore, the possibility of such mechanisms should be systematically considered
497 when interpreting the observations in other regions.

498

499 **Acknowledgments** We thank Chunli Dai and Ian Howat for providing lava field thickness
500 data constructed from the optical survey data. We also thank the European Space Agency for
501 providing Sentinel-1A images.

502 **Funding** This work was supported by grant №14.W03.31.0033 of the Ministry of Education
503 and Science "Geophysical research, monitoring and forecasting of catastrophic geodynamic
504 processes in the Russian Far East" and by the European Research Council under the European
505 Union Horizon 2020 research and innovation program (Grant Agreement 787399-SEISMAZE).

506

507

508

509

References

- 510
511 Belousov, A., Belousova, M., Edwards, B., Volynets A., Melnikov, D., 2015. Overview of the
512 precursors and dynamics of the 2012–13 basaltic fissure eruption of Tolbachik Volcano,
513 Kamchatka, Russia. *Journal of Volcanology and Geothermal Research*. 307 (2015) 22–37.
514 DOI: <http://dx.doi.org/10.1016/j.jvolgeores.2015.04.009>.
- 515 Berardino, P., Fornaro, G., Lanari, R., & Sansosti, E., 2002. A new algorithm for surface
516 deformation monitoring based on Small Baseline Differential SAR Interferograms. *IEEE*
517 *Transactions on Geoscience and Remote Sensing*, 40(11), 2375–2383.
- 518 Briole, P., Massonnet, D., and Delacourt, C., 1997. Post-eruptive deformation associated with the
519 1986–87 and 1989 lava flows of Etna detected by radar interferometry, *Geophys. Res. Lett.*,
520 24(1), 37–40, doi:10.1029/96GL03705.
- 521 Carrara, A., Pinel, V., Bascou, P., Chaljub, E., and De la Cruz-Reyna, S., 2019. Post-emplacement
522 dynamics of andesitic lava flows at Volcán de Colima, Mexico, revealed by radar and optical
523 remote sensing data, *Journal of Volcanology and Geothermal Research*, 381, 1-15,
524 <https://doi.org/10.1016/j.jvolgeores.2019.05.019>.
- 525 Chaussard, E., 2016. Subsidence in the Parícutin lava field: Causes and implications for
526 interpretation of deformation fields at volcanoes, *J. Volcanol. Geotherm. Res.*, 320, 1–11,
527 doi:10.1016/j.jvolgeores.2016.04.009.
- 528 Chen, Y., Zhang, K., Froger, J.-L., Tan, K., Remy, D., Darrozes, J., Peltier, A., Feng, X., Li, H.,
529 and Villeneuve, N., 2018. Long-Term Subsidence in Lava Fields at Piton de la Fournaise
530 Volcano Measured by InSAR: New Insights for Interpretation of the Eastern Flank Motion,
531 *Remote Sensing*, 10(4), 597, doi:10.3390/rs10040597.
- 532 Coppola, D., Marco, L., Massimetti, F., Hainzk, S., Schevchenko, A.V., Mania, R., Shapiro, N.M.,
533 Walter, T.R., 2021. Thermal remote sensing reveals communication between volcanoes of
534 the Klyuchevskoy Volcanic Group. *Sci Rep* 11, 13090. [https://doi.org/10.1038/s41598-021-](https://doi.org/10.1038/s41598-021-92542-z)
535 [92542-z](https://doi.org/10.1038/s41598-021-92542-z)
- 536 Dai, C., Howat, I.M., 2017. Measuring lava flows with ArcticDEM: Application to the 2012–2013
537 eruption of Tolbachik, Kamchatka. *Geophysical Research Letters*, 44, 12,133–12,140.
538 <https://doi.org/10.1002/2017GL075920>
- 539 Danyushevsky, L.V, Plechov, P., 2011. Petrolog3: Integrated software for modeling crystallization
540 processes. *Geochemistry, Geophysics, Geosystems*. Jul; 12(7),
541 <https://doi.org/10.1029/2011GC003516>
- 542 Dvigalo, V. N., I. Yu Svirid, and A. V. Shevchenko. "The first quantitative estimates of parameters
543 for the Tolbachik Fissure Eruption of 2012–2013 from aerophotogrammetric observations."
544 *Journal of Volcanology and Seismology* 8.5 (2013): 261-268.

545 Edwards, B.R., Belousov, A., Belousova, M., Volynets, A., 2015. Introduction to the 2012–2013
546 Tolbachik eruption special issue, *Journal of Volcanology & Geothermal Research.*, 307, 1-
547 2, DOI: 10.1016/j.jvolgeores.2015.12.001

548 Fedotov, S.A. (Ed.) 1984. Great fissure Tolbachik eruption. Kamchatka. 1975-1976. Moscow,
549 Nuaka, 637 p.

550 Fedotov, S., Zharinov, N., Gontovaya, L., 2010. The magmatic system of the Klyuchevskaya
551 group of volcanoes inferred from data on its eruptions, earthquakes, deformation, and deep
552 structure. *Journal of Volcanology and Seismology*, 4(1), 1–33.
553 doi:10.1134/S074204631001001X

554 Fernández, J., Pepe, A., Poland, M. P., & Sigmundsson, F., 2017. Volcano geodesy: Recent
555 developments and future challenges. *Journal of Volcanology and Geothermal Research*, 344,
556 1–12. <https://doi.org/10.1016/j.jvolgeores.2017.08.006>

557 Ferretti A., Prati C., Rocca F., 2001. Permanent scatterers in SAR interferometry //IEEE
558 Transactions on geoscience and remote sensing. v. 39 (1). pp. 8-20.

559 Gordeev, E.I. and Dobretsov, N.L. (eds.), 2017. 2012-2013 Tolbachik Fissure Eruption (TFE-50),
560 Novosibirsk, Izd. SB RAS, p. 427.

561 Hanssen, R.F., 2001. Radar Interferometry: Data Interpretation and Error Analysis. Dordrecht:
562 Kluwer Academic Publishers. 308 p.

563 Hidaka, M., Goto, A., Umino, S., & Fujita, E., 2005. VTFS project: Development of the lava flow
564 simulation code LavaSIM with a model for three-dimensional convection, spreading, and
565 solidification. *Geochemistry, Geophysics, Geosystems*, 6(7).

566 Ji, L., Lu, Z., Dzurisin, D., Senyukov, S., 2013. Pre-eruption deformation caused by dike intrusion
567 beneath Kizimen volcano, Kamchatka, Russia, observed by InSAR. *Journal of Volcanology
568 and Geothermal Research* 256, pp. 87-95.

569 Ji, L., Izbekov, P., Senyukov, S., Lu, Z., 2018. Deformation patterns, magma supply, and magma
570 storage at Karymsky Volcanic Center, Kamchatka, Russia, 2000–2010, revealed by InSAR.
571 *Journal of Volcanology and Geothermal Research.* v. 352. pp. 106-116.

572 Keszthelyi, L., Denlinger, R., 1996. The initial cooling of pahoehoe flow lobes, *Bull. Volcanol.*,
573 58, 5 – 18.

574 Koulakov, I., Shapiro, N. M., Sens-Schönfelder, C., Luehr, B. G., Gordeev, E. I., Jakovlev, A.,
575 Abkadyrov, I., Chebrov, D. V., Bushenkova, N., Droznina, S. Y., Senyukov, S. L.,
576 Novgorodova, A., Stupina, T., 2020. Mantle and crustal sources of magmatic activity of
577 Klyuchevskoy and surrounding volcanoes in Kamchatka inferred from earthquake
578 tomography. *Journal of Geophysical Research: Solid Earth*, 125, e2020JB020097.
579 <https://doi.org/10.1029/2020JB020097>

580 Kubanek, Julia, et al. "Lava flow mapping and volume calculations for the 2012–2013
581 Tolbachik, Kamchatka, fissure eruption using bistatic TanDEM-X InSAR." *Bulletin of*
582 *Volcanology* 77.12 (2015): 1-13.

583 Kubanek, Julia, Malte Westerhaus, and Bernhard Heck. "TanDEM-X time series analysis reveals
584 lava flow volume and effusion rates of the 2012–2013 Tolbachik, Kamchatka fissure
585 eruption." *Journal of Geophysical Research: Solid Earth* 122.10 (2017): 7754-7774.
586

587 Lanari, R., Mora, O., Manunta, M., Mallorqui, J. J. , Berardino, P., Sansosti, E., 2004. A small-
588 baseline approach for investigating deformations on full-resolution differential SAR
589 interferograms. In: *IEEE Transactions on Geoscience and Remote Sensing*, vol. 42, no. 7,
590 pp. 1377-1386; doi: 10.1109/TGRS.2004.828196.

591 Lundgren, P., Kiryukhin A., Milillo P., Samsonov S., 2015. Dike model for the 2012–2013
592 Tolbachik eruption constrained by satellite radar interferometry observations, *J. Volcanol.*
593 *Geotherm. Res.* <http://dx.doi.org/10.1016/j.jvolgeores.2015.05.011>

594 Lundgren, P., Lu, Z., 2006. Inflation model of Uzon caldera, Kamchatka, constrained by satellite
595 radar interferometry observations. *Geophysical Research Letters*. v. 33(6).

596 Mania, R., Walter, T. R., Belousova, M., Belousov, A., & Senyukov, S. L. (2019). Deformations
597 and morphology changes associated with the 2016–2017 eruption sequence at Bezymianny
598 Volcano, Kamchatka. *Remote Sensing*, 11(11), 1278.

599 Mikhailov, V.O., Volkova, M.S., Timoshkina, E.P., Shapiro, N.M., and Smirnov, V.B., On the
600 Connection between the Koryaksky Volcano Activation in 2008-2009 and the Underlying
601 Magmatic Processes, *Fiz. Zemli*, 2022 (accepted).

602 Neri, A., 1998. A local heat transfer analysis of lava cooling in the atmosphere: Application to
603 thermal diffusion-dominated lava flows, *J. Volcanol. Geotherm. Res.*, 81, 215– 243.

604 Patrick, M. R., Dehn, J., Dean, K., 2004. Numerical modeling of lava flow cooling applied to the
605 1997 Okmok eruption: Approach and analysis. *Journal of Geophysical Research: Solid*
606 *Earth*, 109(B3).

607 Plechov, P., Blundy, J., Nekrylov, N., Melekhova, E., Shcherbakov, V., Tikhonova, M.S., 2015.
608 Petrology and volatile content of magmas erupted from Tolbachik Volcano, Kamchatka,
609 2012–13. *Journal of Volcanology and Geothermal Research*, 307, pp.182-199.

610 Peck, D. L., 1978. Cooling and vesiculation of Alae lava lake, Hawaii, Tech. rep., U. S. Govt.
611 Print. Off.

612 Poland, M. P., 2014. Time-averaged discharge rate of subaerial lava at Kīlauea Volcano, Hawai‘i,
613 measured from TanDEM-X interferometry: Implications for magma supply and storage

614 during 2011–2013, *J. Geophys. Res. Solid Earth*, 119, 5464–5481,
615 doi:10.1002/2014JB011132.

616 Senyukov, S.L., Mikhailov, V.O., Nuzhdina, I.N., Kiseleva, E.A., Droznina, S.Ya., Timofeeva,
617 V.A., Volkova, M.S., Shapiro, N.M., Kozhevnikova, T.Yu., Nazarova, Z.A., and
618 Sobolevskaya, O.V., Simultaneous Study of Seismicity and Sentinel-1A Data to Assess the
619 Possible Eruption of the Extinct Bolshaya Udina Volcano, *Volcanology and Seismology*,
620 2020, no. 5, pp. 26-39; DOI: 10.31857/S0203030620050053.

621 Shapiro, N.M., Sens-Schönfelder, C., Lühr, B.G., Weber, M., Abkadyrov, I., Gordeev, E.I.,
622 Koulakov, I., Jakovlev, A., Kugaenko, Y.A., & Saltykov, V. A., 2017a. Understanding
623 Kamchatka's extraordinary volcano cluster. *Eos*, 98(7), 12–17. doi:10.1029/2017EO071351

624 Shapiro, N. M., Droznin, D. V., Droznina, S. Y., Senyukov, S. L., Gusev, A. A., & Gordeev, E. I.,
625 2017b. Deep and shallow long-period volcanic seismicity linked by fluid-pressure transfer.
626 *Nature Geoscience*, 10(6), 442– 445. <https://doi.org/10.1038/ngeo2952>

627 Shaw H.R., Hamilton M.S., Peck D.L., 1977. Numerical analysis of lava lake cooling models: Part
628 I, description of the method, *American Journal of Science*, Vol. 277, p. 384-414

629 Wittmann, W., F. Sigmundsson, S. Dumont, and Y. Lavallée, 2017. Post-emplacement cooling
630 and contraction of lava flows: InSAR observations and a thermal model for lava fields at
631 Hekla volcano, Iceland, *J. Geophys. Res. Solid Earth*, 122, 946–965,
632 doi:10.1002/2016JB013444.